Aerodynamic Characterization of New Parachute Configurations for Low-Density Deceleration

Christopher L. Tanner*, Ian G. Clark†, John C. Gallon‡, Tommaso P. Rivellini§
Jet Propulsion Laboratory, California Institute of Technology, Pasadena, CA, 91109, USA

Allen Witkowski¶
Pioneer Aerospace Corporation, South Windsor, CT, 06074, USA

The Low Density Supersonic Decelerator project performed a wind tunnel experiment on the structural design and geometric porosity of various sub-scale parachutes in order to inform the design of the 110 ft nominal diameter flight test canopy. Thirteen different parachute configurations, including disk-gap-band, ringsail, disksail, and starsail canopies, were tested at the National Full-scale Aerodynamics Complex 80- by 120-foot Wind Tunnel at NASA Ames Research Center. Canopy drag load, dynamic pressure, and canopy position data were recorded in order to quantify the relative drag performance and stability of the various canopies. Desirable designs would yield increased drag above the disk-gap-band with similar, or improved, stability characteristics. Ringsail parachutes were tested at geometric porosities ranging from 10% to 22% with most of the porosity taken from the shoulder region near the canopy skirt. The disksail canopy replaced the ringslot portion of the ringsail canopy with a flat circular disk and was tested at geometric porosities ranging from 9% to 19%. The starsail canopy replaced several ringsail gores with solid gores and was tested at 13% geometric porosity. Two disksail configurations exhibited desirable properties such as an increase of 6-14% in the tangential force coefficient above the DGB with essentially equivalent stability. However, these data are presented with caveats including the inherent differences between wind tunnel and flight behavior and qualitative uncertainty in the aerodynamic coefficients.

Nomenclature

A_{ts}	cross-sectional area of the wind tunnel test section
C_m	pitching moment coefficient
C_{m_α}	static pitch stiffness coefficient, $\partial C_m/\partial\alpha$
$C_{m_{\dot\alpha}}$	dynamic pitch damping coefficient, $\partial C_m/\partial\left(\frac{\dot\alpha D_0}{2V}\right)$
C_D	drag force coefficient
C_N	normal force coefficient
C_T	tangential force coefficient
D_0	canopy nominal diameter
D_a	forebody diameter
D_p	parachute projected diameter
F_T	canopy load tangent to the riser
g	acceleration due to gravity

*LDSD NFAC Test Lead, Member AIAA.
†LDSD Principal Investigator, Member AIAA.
‡LDSD Parachute System Cognizant Engineer, Member AIAA.
§LDSD Chief Engineer, Member AIAA.
¶Director of Engineering Operations, AIAA Associate Fellow.

I_{yy}	moment of inertia of the parachute system and apparent mass
k_{44}	apparent inertia coefficient
k_q	blockage correction factor
m_p	parachute mass (including canopy and suspension lines)
M	moment about the point of rotation
q_∞	freestream dynamic pressure
q_c	dynamic pressure corrected for blockage
q_w	resultant dynamic pressure (corrected for canopy motion)
R_{cm}	distance from the point of rotation to the system center of mass
R_{cp}	distance from the point of rotation to the canopy center of pressure
S_0	canopy nominal area
V_c	wind tunnel velocity corrected for blockage
V_t	tangential velocity of the canopy
V_w	resultant wind velocity (corrected for canopy motion)
V_∞	freestream wind velocity
α_G	total geometric angle
α_T	total angle of attack
$\Delta\alpha$	change in angle of attack due to canopy motion
Δq	change in dynamic pressure due to blockage
ϕ	clock angle of the canopy projected into the yz-plane
γ	angle between the freestream wind vector and the velocity vector tangent to the parachute's arc of motion
λ_G	geometric porosity
λ_T	total porosity
ψ	yaw Euler angle
ρ_∞	freestream air density
θ	pitch Euler angle
Ω	canopy angular velocity magnitude
AoA	angle of attack
cm	center of mass
cp	center of pressure
DAS	data acquisition system
DGB	disk-gap-band
DS	disksail
LDSD	Low Density Supersonic Decelerator
MER	Mars Exploration Rover
MSL	Mars Science Laboratory
NFAC	National Full-scale Aerodynamics Complex
PIA	Parachute Industry Association
PEPP	Planetary Entry Parachute Program
RS	ringsail
SS	starsail

I. Introduction

THE Low Density Supersonic Decelerator (LDSD) project is developing a new decelerator system for Mars entry that includes an inflatable aerodynamic decelerator and a new 33.5 m (110 ft) nominal diameter supersonic parachute. Given the success of the disk-gap-band (DGB) supersonic parachute on previous missions to the surface of Mars, the onus is on LDSD to ensure that the new parachute system provides measurable improvements in drag with equivalent or better stability than that of the DGB at both supersonic and subsonic Mach numbers.

To help inform the design of this new parachute, a wind tunnel test program was executed using sub-scale canopies of various structural configurations, geometric porosities, and porosity distributions. Two DGB canopies constructed from two broadcloth materials with different permeabilities were tested to obtain reference performance criteria. Ringsail and two unique, ringsail-derivative canopies with various magnitudes and distributions of geometric porosity were also tested. Geometric porosities of the ringsail and ringsail-derivative canopies varied from approximately 9% to 21%. These canopies were also constructed from F-111 nylon, thus the geometric porosity was essentially equal to the total porosity.

The goal of this wind tunnel test was to quantify the relative drag and stability between various ringsail-based canopies and compare their performance against the DGB performance. Load cell data were collected to quantify the tangential force (oriented along the parachute axis of symmetry), which acts as a surrogate for the drag force (oriented along the wind vector) in this study. Dynamic pressure data were collected both upstream and downstream of the test article to help determine blockage effects. The three-dimensional position of the canopy vent was tracked with respect to the point of rotation using stereo photogrammetry. These photogrammetric data produced a statistical distribution of the angles of attack and allowed for correlation of the canopy load with the angle of attack. Additionally, a reverse parameter identification method was applied to the photogrammetric data to estimate the static and dynamic stability coefficients and the trim angle of attack of each of the canopies.

The canopies were tested at relatively low freestream wind speeds, approximately 15 kts (25 ft/s) and 25 kts (42 ft/s), to maximize the lifetime of the test articles, permit personnel in the test section while taking data, and limit loads to within the load cell's acceptable range. At these wind speeds, significant oscillation and relatively high angular rates were observed for the low geometric porosity / high drag canopies. Additional geometric porosity was created by removing sail panels at strategic locations in the ringsail and disksail canopies. Increased geometric porosity generally increased stability and decreased drag performance, as would be expected. However, canopy performance differed slightly for equivalent magnitudes of porosity depending on the canopy configuration and the distribution of the geometric porosity.

II. Test Setup and Operation

A. Wind Tunnel Facility

Testing was conducted at the National Full-scale Aerodynamics Complex (NFAC) 80- by 120-foot Wind Tunnel (80x120), located at the NASA Ames Research Center. The fan drive system consists of six, 40 ft diameter electrical fans, each with a peak output of 22,500 horsepower and variable pitch blades, which are capable of generating wind speeds up to 100 kts in the 80x120 test section. The fan drive system and part of the tunnel circuit are shared with a 40- by 80-foot test section in the same complex, which is capable of 300 knot wind speeds. The NFAC facility is shown in Fig. 1a, with the 80x120 inlet and test section seen in the foreground. The fan drive system is shown in Fig. 1b.

The model support system used for this test was nearly identical to that used during the Space Shuttle Orbiter drag parachute test in 1993.[1] The parachutes were supported at tunnel centerline by a 40 ft tall strut that was equipped with a ball joint at its apex. A fairing was installed around the strut to reduce flow turbulence. The Space Shuttle Orbiter drag chute load weldment and socket were reused for this wind tunnel test, although slight modifications were made to the weldment to accommodate the load cell and a counterweight. Since the LDSD parachute would ultimately be operating behind a relatively large blunt body, an approximately 7 ft diameter forebody simulator was fabricated, mounted on top of the fairing, and axially aligned with the strut ball. The strut, forebody, and fairing are shown in Fig. 2 with a DGB parachute in flight.

To mimic the relative dimensions of the LDSD supersonic flight vehicle, the forebody was placed approximately 3 ft in front of the strut ball. Similarly, a 3 ft riser and parachute swivel were attached to the load

(a) Facility ariel view

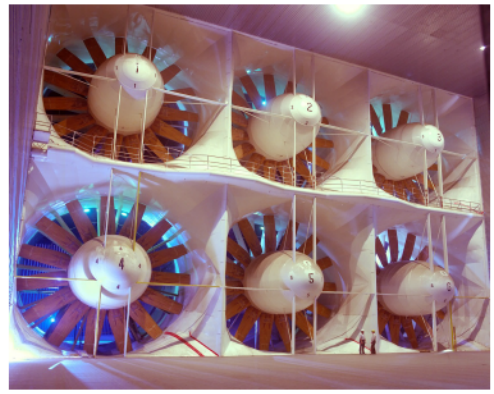

(b) Fan drive system

Figure 1: Images of the NFAC facility and fan drive system.

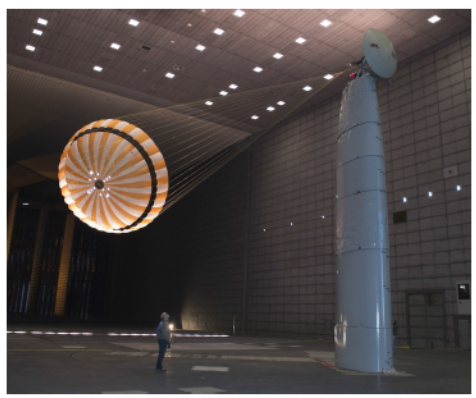

Figure 2: 40 ft strut with fairing and forebody in the 80x120 test section.

weldment to obtain an appropriately scaled parachute trailing distance. Dimensions of the model support hardware and test articles are shown in Fig. 3.

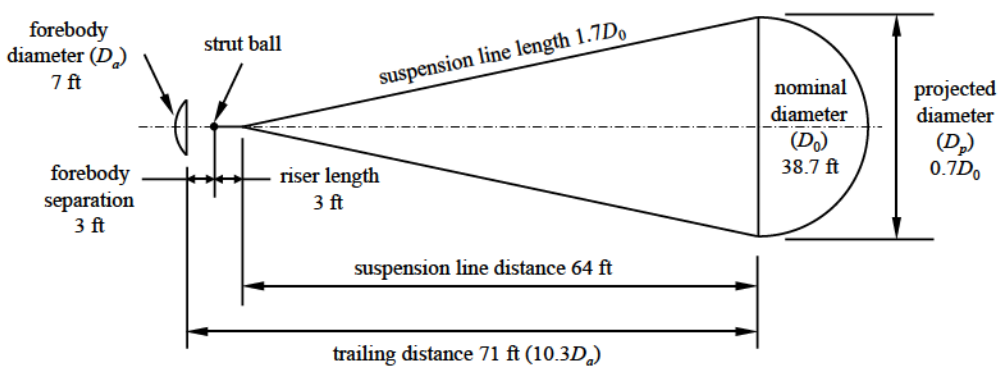

Figure 3: Major dimensions of the model support system and test articles. All indicated dimensions are approximate and are approximately 35.2% of the full-scale flight system.

B. Test Articles

Four primary types of canopies were tested during this wind tunnel test program. The geometric porosity distribution was the key design parameter, which drove the primary canopy designs and their subsequent

modifications. Geometric porosity (λ_G) is the ratio of the open area of a parachute canopy to its nominal area. Note that for a parachute, the nominal area includes all of the fabric acreage as well as any open areas within the canopy. For example, the gap area in a DGB is included in its nominal area and the open area created by sail fullness is included in the nominal area of a ringsail. Geometric porosity and its calculation with respect to a ringsail canopy are described further by Witkowski et al.[2]

DGB canopies were tested in order to establish a baseline performance reference and assess the goodness of the other canopy designs relative to the current state-of-the-art. The other three canopy types included a traditional ringsail canopy and two unique designs referred to as a disksail and a starsail. The ringsail test articles were a sub-scale version of the ringsail canopy used in the high-altitude subsonic parachute test conducted by JPL in 2004.[3] The disksail replaced 11 rings around the apex of the ringsail canopy with a flat circular disk. The goal of the disksail was to recover the geometric porosity in the canopy apex to increase drag, move the recovered porosity elsewhere in the canopy to enhance stability, and simultaneously make the parachute lighter in weight by eliminating a portion of the ringsail structure. To recover geometric porosity in a different way, the starsail replaced 24 ringsail gores with solid gores in a six-finger pattern and the sails in rings 17 through 20 were slightly shortened to increase porosity around the shoulder of the canopy. Each of the four main parachute structural configurations considered for this test are described in Table 2.

Table 2: Major test article canopy configurations.

Canopy Type	disk-gap-band	ringsail	disksail	starsail
Image		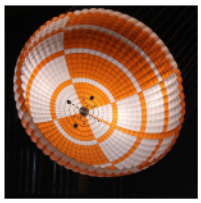		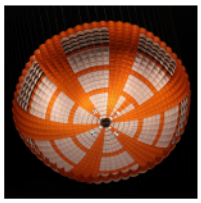
No. of Gores	40	60	60	60
Vent Dia. (ft)	2.5	1.5	2.0	2.1
Features	28 ft dia flat disk, 1.6 ft gap height, 4.7 ft band height	22 rings	11 rings, 18.1 ft dia flat disk	24 flat circular gores, 36 ringsail gores, 22 rings, 28.1 ft^2 gap in rings 17-20
Geometric Porosity	13%	10%	9%	13%

LDSD selected a combination of 1.17 oz/yd^2 PIA-C-44378 "F-111" nylon and 1.9 oz/yd^2 Diamond Weave nylon as the candidate broadcloth materials for the sails and the crown of the full-scale parachute, respectively. These materials have been calendared to considerably reduce their permeability. For example, F-111 nylon has a nominal permeability less than 5 $ft^3/min/ft^2$ at 0.5" H_2O pressure (approximately 5.2 psf) per its specification. However, these materials differ from the material used to build the DGB parachutes for the Mars Exploration Rover (MER), Mars Phoenix Scout, and Mars Science Laboratory (MSL) missions. Those parachutes were constructed from 1.1 oz/yd^2 MIL-C-7020 Type I nylon, which has a nominal permeability less than 100 $ft^3/min/ft^2$ at 0.5" H_2O pressure per its specification. Low-permeability nylon materials were selected by LDSD instead of high-permeability for a number of reasons.[4] In particular, it was demonstrated that the material permeability causes a significant difference in the flight behavior of a parachute canopy in a high-density, high-Reynolds number environment.[5] Additionally, it has been shown that the material permeability has a negligible effect on the total porosity of the canopy in a low-density, low-Reynolds number environment, effectively making the total porosity equal to the geometric porosity.[6] The use of a low-permeability broadcloth material can help reduce uncertainties in the parachute performance and behavior between low-altitude Earth-based (high-density atmosphere) parachute testing and the parachute flight at Mars (low-density atmosphere). As such, all of the canopies in this test program were constructed from F-111 nylon unless otherwise stated.

Each of the test articles measured 11.8 m (38.7 ft) nominal diameter and utilized 65.8 ft long ($1.7D_0$)

suspension lines. The test articles were approximately 35.2% of full-scale, assuming a 33.5 m (110 ft) nominal diameter full-scale canopy (excluding the DGB canopies). The test article size was selected because the full-scale Mars Phoenix DGB measured 38.7 ft nominal diameter and was immediately available for testing. This allowed the LDSD parachute performance to be directly compared against a DGB canopy that was known to have performed well in a Mars flight environment. Additionally, a 38.7 ft nominal diameter canopy permitted approximately ±20° of freedom in the vertical plane and ±30° of freedom in the horizontal plane of the test section. These angle limitations were assumed to be sufficiently large given historically measured angles of attack for DGB canopies.

It should be noted that the test articles were not mass-scaled and were designed to withstand loads greatly in excess of the expected wind tunnel loads. Due to financial and schedule constraints, it was necessary to fabricate the test articles from existing broadcloth material to be used for the full-scale 150,000 lb_f LDSD canopy. Structural tapes and suspension lines used to construct the three "sail" canopies were stiffness scaled to obtain a more accurate projected diameter, but the structural components still have excessive load capability (and thus excessive mass). Additionally, the DGB structural components were not scaled from the Phoenix flight limit load specification of 12,700 lb. As such, the relative sub-scale canopy masses are not representative of an equivalent full-scale system and are not presented in order to avoid confusion.

Throughout the test program, the geometric porosity of the "sail" canopies was modified by removing sail panels at various places on the canopy. It was believed that strategic distribution of the geometric porosity could optimize the drag and stability of the parachute. These modifications and their effects are described in Section IV.

C. Instrumentation

As previously stated, the objective of this test program was to quantify the relative drag and stability of various canopy types. To accomplish this objective, three primary measurements were acquired: canopy tagnetial load (along the riser), dynamic pressure, and the canopy position within the test section. A 5,000 lb_f uniaxial load cell was mounted to the load weldment to measure the canopy tangential force, which was acquired at a frequency of 1,000 Hz. T
which was connected to the load cell via
was not anticipated, a parachute swivel
occur. The load train through the load

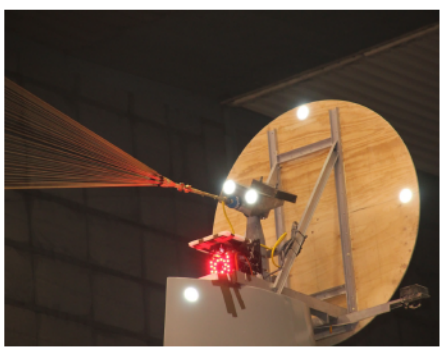

(a)

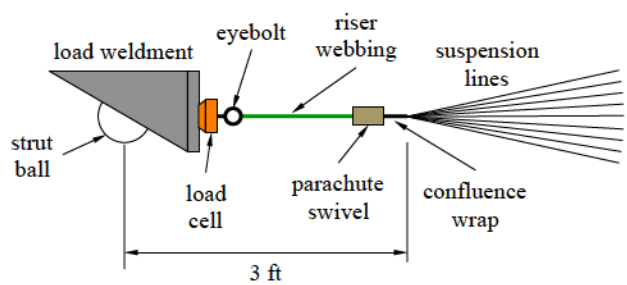

(b)

Figure 4: Photo and diagram of the model support system load train.

Four separate dynamic pressure measurements were taken at four places in the test section to help quantify the blockage caused by the parachute and ensure proper non-dimensionalization of the force coefficients. The wind tunnel standard dynamic pressure was recorded as an average of four pitot probes located on the floor, ceiling, and side walls at tunnel centerline slightly upstream of the beginning of the test section. In addition to the standard dynamic pressure measurement, three independent "q-probes" were located at three different positions in the test section. The q-probes consisted of co-located pitot probes and pressure transducers mounted on 6 ft tall modified microphone stands. The north q-probe was stationed upstream of the strut near the beginning of the test section to corroborate the standard wind tunnel measurements using independent hardware. The other two q-probes were stationed downstream of the canopy approximately 7 ft from the east and west walls of the test section. The purpose of these q-probes was to measure the dynamic

Chris Tanner
September 2012

pressure downstream of the test articles and help quantify the blockage effects. Dynamic pressure data was acquired at 1,000 Hz. The q-probes and their placement in the test section are shown in Fig. 5.

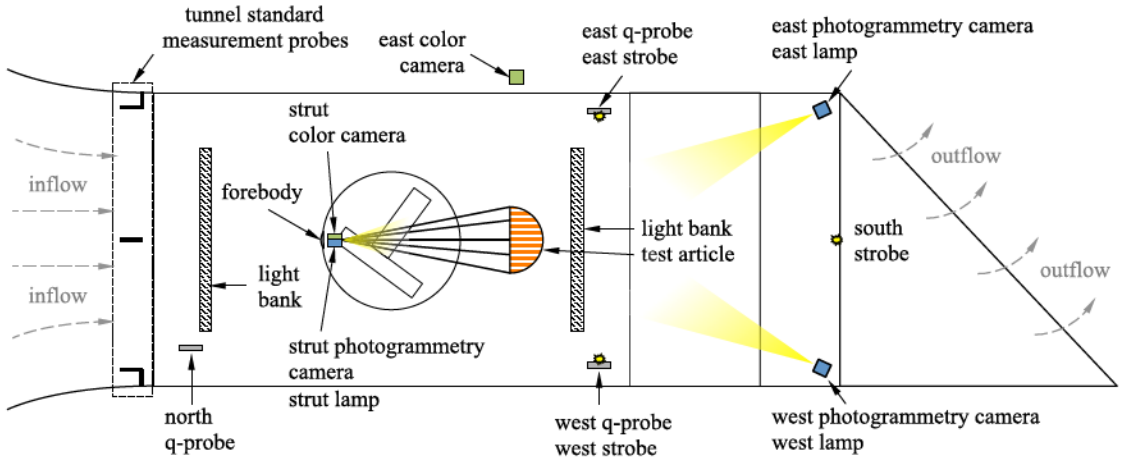

Figure 5: Test section equipment layout.

The canopy was tracked using a photogrammetry system to obtain an accurate measurement of its position in three-dimensional space. Three synchronized, high-resolution cameras recorded images of matching retro-reflective fiducial targets on both the inside and outside surfaces of each canopy at 60 frames per second. Two of these cameras were located downstream of the canopy on the floor of the diffuser at the positions indicated in Fig. 5 and were used in stereo to generate the position measurements. The third camera was located on the strut just below the strut ball and viewed the inside of the canopies. It provided a secondary estimate of the canopy position based on a simple linear scaling between image and object space.[7] The strut camera also captured strobe flashes from the two downstream q-probes and the debris fence that were required to synchronize the photogrammetric measurements with the load cell measurements. All three cameras were calibrated prior to the test by distributing targets in the test section and in the region of interest whose space coordinates were precisely known and acquiring images of them with all three cameras. A view from each of the photogrammetry cameras is shown in Fig. 6.

(a) West camera (b) East camera (c) Strut camera

Figure 6: Monochromatic images of a test article recorded by the photogrammetry cameras. The retro-reflective fiducial pattern was specifically designed to maximize light return and help automate target location.

Two high-resolution (1080p) color cameras were also used to collect video data of the canopies. These cameras were located in the east wall perpendicular to the canopy and adjacent to the photogrammetry camera on the strut, as shown in Fig. 5. Given the low-light / high-contrast images from the photogrammetry cameras, these video data were used as the primary video data for this test series. Representative images from the two color video cameras are shown in Fig. 7.

(a) East color camera (showing strobe flash)

(b) Strut color camera

Figure 7: Images from the color cameras in the NFAC east wall and on the strut.

D. Test Conditions and Operations

Testing was performed at only two wind speeds: approximately 15 kts (25 ft/s) and 25 kts (42 ft/s). The wind speed of 25 kts resulted in peak loads of approximately 5,000 lb_f for the ringsail and disksail parachutes. Additionally, wind speeds below 30 knots allowed personnel to remain in the test section while taking data to directly observe and photograph the parachute behavior while in flight. Finally, with knowledge that the canopies would likely see several hours of flight time, a relatively low wind speed of 25 kts increased confidence that the test articles would have a sufficient life span. The 15 kt wind speed was tested to determine if there was a dynamic pressure effect on the canopy aerodynamics, but still allowed the canopy to remain at or near the tunnel centerline (on average).

Unlike the prior MER and MSL parachute testing in the 80x120 test section, the canopies were never mortar deployed. All of the canopies were statically inflated from the floor of the test section, as shown in Fig. 8a. Data point durations were either 3 or 6 minutes in length. Long sample durations permitted many canopy oscillations to be captured and ensured that the overall canopy behavior was recorded. The collection of a sufficient amount of data was particularly critical in calculating the stability coefficients (see Section III.D) where the quality and accuracy of these data increase with the amount of data present to estimate the parameters.

Since only a limited number of test articles could be fabricated and many geometric porosity distributions were to be investigated, sail panels were strategically removed from existing ringsail and disksail test articles to alter the parachute's geometric porosity. Modification of the test articles involved simply cutting sail panels out of the canopy structure with scissors, as shown in Fig. 8b. Only the broadcloth material was removed from the canopy; the structural tapes were left in place.

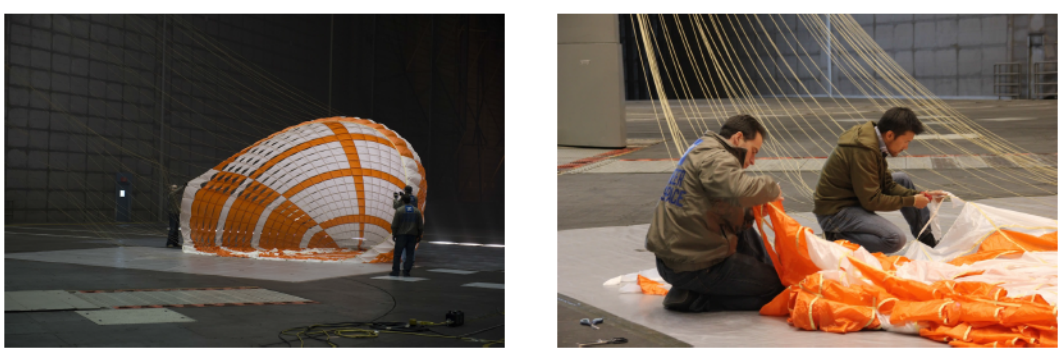

(a) Static inflation

(b) Sail panel removal

Figure 8: Test operation and canopy modification by JPL and Pioneer personnel.

III. Data Analyses

A. Angle of Attack Correction

The total angle of attack (α_T) is a more appropriate aerodynamic angle for an axisymmetric body instead of the more traditional angle of attack (AoA) and sideslip angle convention for aircraft. The total AoA is defined as the angle between the wind vector and the parachute axis of symmetry. For a static parachute position in the wind tunnel, the total AoA is equal to the total geometric angle (α_G), which is defined as the angle between the tunnel centerline and the line between the ball joint and the center of the canopy vent (essentially the parachute riser line). For a parachute moving in the wind tunnel, the tangential velocity of the canopy along its arc of motion augments the total wind velocity on the canopy, subsequently making the total AoA different from the total geometric angle. Additionally, the total AoA is dependent on the direction in which the canopy is moving – i.e. if the canopy is moving away from centerline (referred to as "advancing") or towards centerline (referred to as "retreating"). The differences between α_G and α_T for the static, advancing, and retreating canopy cases are shown in Table 9. The total AoA is calculated as in Eq. (1), where the direction of the arrow for $\Delta\alpha$ in Table 9 indicates whether it is added to (arrows pointed in the same direction), or subtracted from (arrows pointed in opposite directions), α_G. Additional details on how the angle correction was performed is presented in reference 8.

$$\alpha_T = \alpha_G \pm \Delta\alpha \tag{1}$$

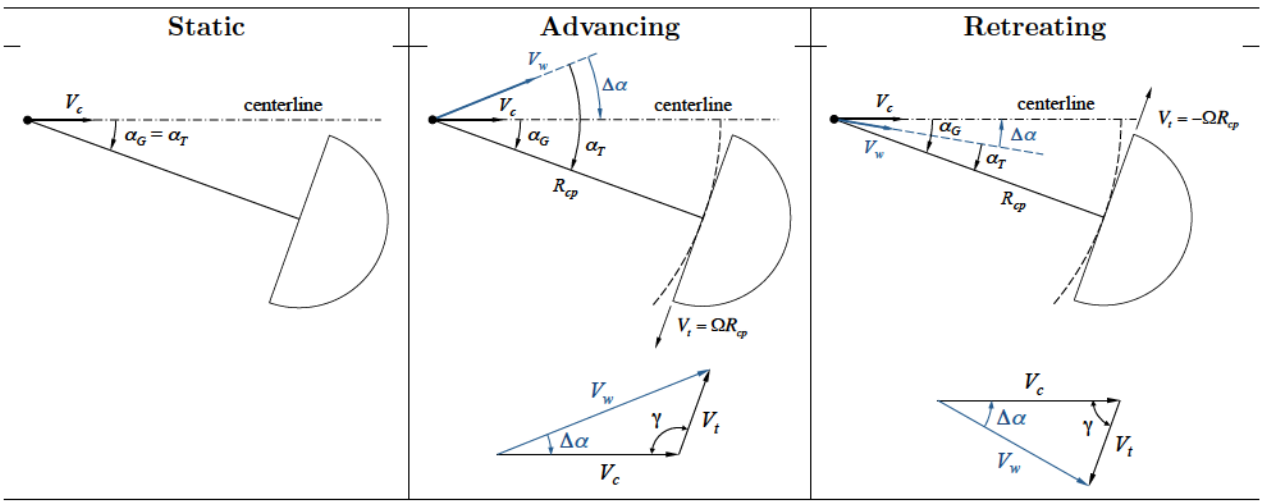

Figure 9: Diagram of the total angle of attack (α_T) versus the total geometric angle (α_G) for static, advancing, and retreating canopies.

Canopy motion in the wind tunnel has two important, but non-intuitive, effects on the canopy's total AoA. First, the maximum total AoA is greater than the maximum total geometric angle, meaning that the parachute is actually seeing higher total angles of attack than is being physically exhibited in the wind tunnel. Second, 0° total AoA does not occur when the parachute is in the center of the test section. Per the diagram in Table 9, 0° total AoA actually occurs at some non-zero total geometric angle when the canopy is retreating. In fact, the maximum total AoA for a parachute in motion will occur near where the tangential velocity is maximum, which is near $\alpha_G = 0°$. Thus, the maxima of α_G and α_T are almost 180° out of phase from each other. The shift in the distribution and range due to the angle of attack correction is illustrated in Figures 10a and 10b. The mean and 95th percentile angles are shown in red on the histograms to help quantify the angular shift. Figure 10c illustrates how the maximum total angles of attack occur near the lower total geometric angles and vice versa. Finally, Fig. 10d shows a trace of the vent position to indicate its motion about the wind tunnel test section during the data sample.

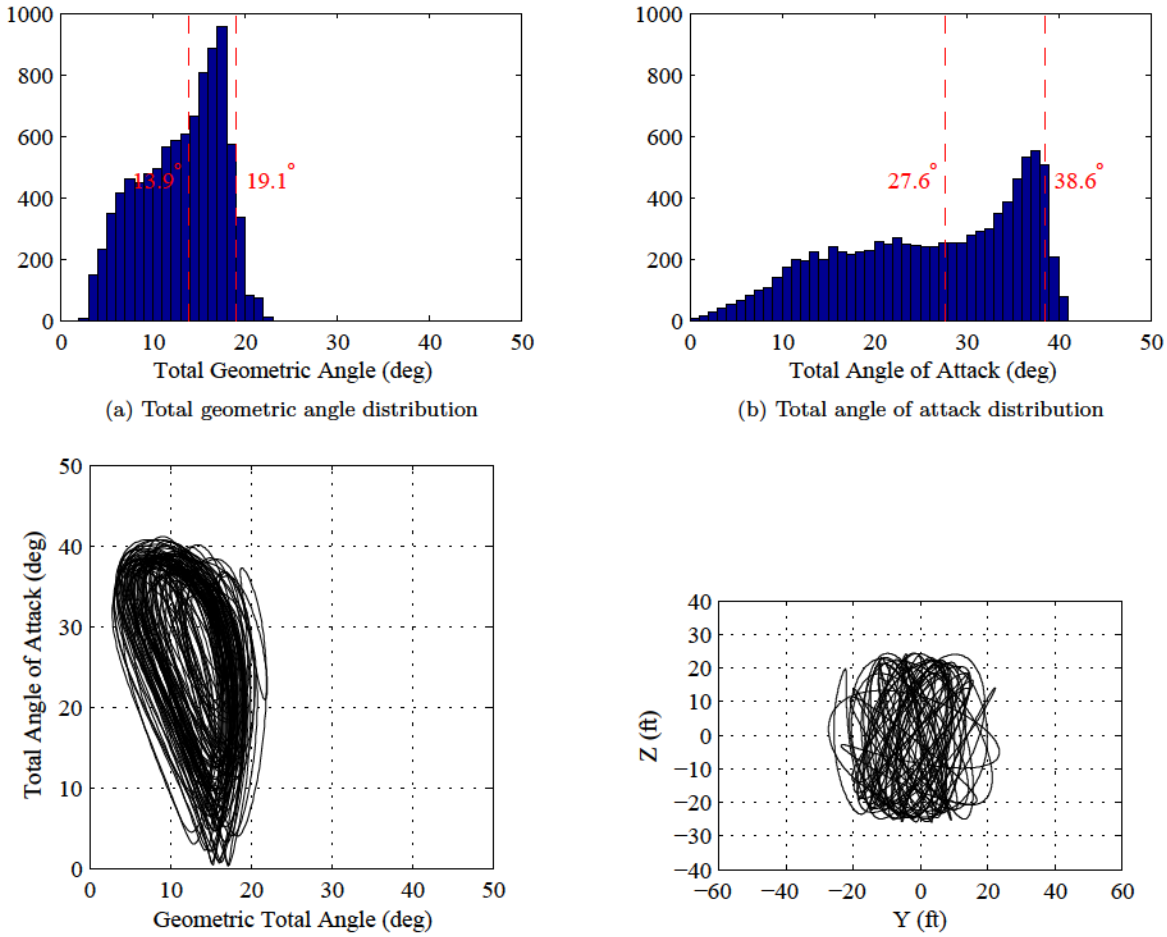

(a) Total geometric angle distribution

(b) Total angle of attack distribution

(c) α_T relative to α_G

(d) Trace of vent position in the test section

Figure 10: Representative angle correction data for the ringsail canopy. The mean and 95th percentile angles are shown in red on the histograms.

B. Velocity Correction

The velocity triangles in Table 9 illustrate how the resultant wind velocity (V_w) changes depending on whether the canopy is advancing or retreating. The resultant velocity is greater than the blockage-corrected velocity (V_c) if the canopy is advancing and less than the blockage-corrected velocity if the canopy is retreating. It is important to capture this effect when reducing the force coefficients since the canopy forces are not only changing with the angle of attack, but are also changing due to the increase and decrease in dynamic pressure associated with the canopy's advancing and retreating motion.

Aerodynamic forces are theoretically applied at the canopy center of pressure (cp), which is located at a distance R_{cp} from the strut ball joint. For the DGB canopy, the cp is located very near the skirt of the canopy.[5] Thus, the resultant velocity must be calculated at the canopy skirt in order to properly reduce the aerodynamic coefficients. The resultant velocity vector at the cp is given in Eq. (2). The velocity components of the cp are given in terms of the canopy Euler angles and angular rates in Eq. (3). The canopy is rotated first through the pitch angle (θ), then through the yaw angle (ψ) as shown in Fig. 11.

$$V_w = \sqrt{(V_c - \dot{x}_{cp})^2 + \dot{y}_{cp}^2 + \dot{z}_{cp}^2} \tag{2}$$

$$\mathbf{\Omega} \times \mathbf{R_{cp}} = \begin{bmatrix} \dot{x}_{xp} \\ \dot{y}_{cp} \\ \dot{z}_{cp} \end{bmatrix} = R_{cp} \begin{bmatrix} -\dot{\theta}\sin\theta\cos\psi - \dot{\psi}\cos\theta\sin\psi \\ \dot{\psi}\cos\psi \\ -\dot{\theta}\cos\theta\cos\psi + \dot{\psi}\sin\theta\sin\psi \end{bmatrix} \tag{3}$$

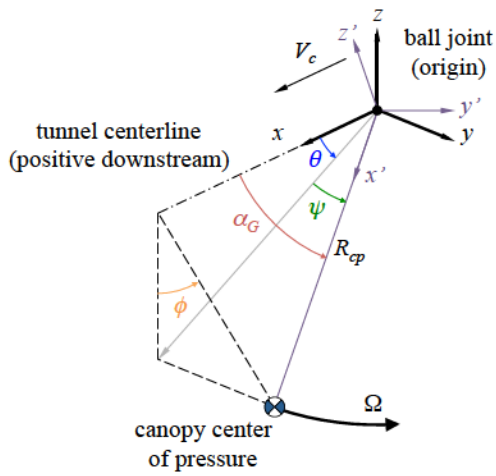

Figure 11: Test section coordinate system (x, y, z) is shown with the origin at the ball joint, positive x-axis pointing downstream along the tunnel centerline, and positive z-axis pointing upwards (opposite of the gravity direction). The tunnel wind velocity V_c is oriented parallel with the x-axis. The canopy coordinate system (x', y', z') is shown with the x'-axis pointing along the riser towards the canopy vent and has been rotated first by the pitch angle θ and second by the yaw angle ψ. The canopy coordinate system is rotating about the origin at an angular velocity Ω. The geometric total angle α_G and the clock angle ϕ are also defined.

C. Dynamic Pressure and Blockage

The usable cross-sectional area of the test section (A_{ts}) is 9,345.7 ft (118.3x79 ft) and the projected area of the parachutes was approximately 560.4 ft, resulting in a geometric blockage of 6%. This level of geometric blockage in a wind tunnel is not insignificant and the effects caused by the wind tunnel walls needed to be considered. The presence of solid wind tunnel test section walls can cause increased dynamic pressure locally around the test article due to flow constriction. Prior to testing, two analytical methods were used to estimate blockage effects, which subsequently translated into estimates of peak expected parachute drag and a pressure range for the downstream q-probes. Maskell[9] and Macha and Buffington[10] developed empirical methods to calculate the blockage effects of a bluff body in a rectangular test section with solid walls. Both methods relied on the general expression in Eq. (4), however both methods use different blockage factors k_q.

$$\frac{\Delta q}{q} = k_q \frac{C_D S_0}{A_{ts}} \tag{4}$$

Maskell concluded a k_q value of 2.5 based on flow theory and experimental data of flat plates normal to the wind stream. Macha and Buffington investigated the blockage associated with parachutes of varying diameters and geometric porosity and concluded a k_q value of 1.85 that was independent of canopy porosity. Assuming a C_D of 0.85 (based on the range given by Knacke for ringsail parachutes[11]), the increase in dynamic pressure ranges from 12.7% to 9.4% based on Maskell and Macha methods, respectively. Previous wind tunnel tests of parachutes[1,5,12] all used Macha's method to correct for blockage. However, a 12.7% increase in the dynamic pressure (Maskell's method) was assumed for the present test out of conservatism.

The freestream dynamic pressure (q_∞) was measured by the upstream tunnel standard measurement probes shown in Fig. 5. The downstream q-probes provided a direct measurement of the dynamic pressure downstream of the test articles (q_c). These measurements were taken, in part, to compare actual pressure measurements against the empirical theories developed by Maskell and Macha and Buffington. Ideally, the measurements should have been taken very near the canopy skirt instead of slightly downstream. However, positioning the q-probes further upstream posed unacceptable risk to the operation crew in the test section and the test articles.

Finally, the dynamic pressure on the canopy increased due to its tangential velocity. The resultant dynamic pressure due to the canopy's oscillatory motion was calculated using Eq. (5). This dynamic

pressure captures the effect of blockage as well as the effect of the tangential velocity of the canopy, thus this dynamic pressure is used to non-dimensionalize the aerodynamic coefficients.

$$q_w = \frac{1}{2}\rho_\infty V_w^2 \tag{5}$$

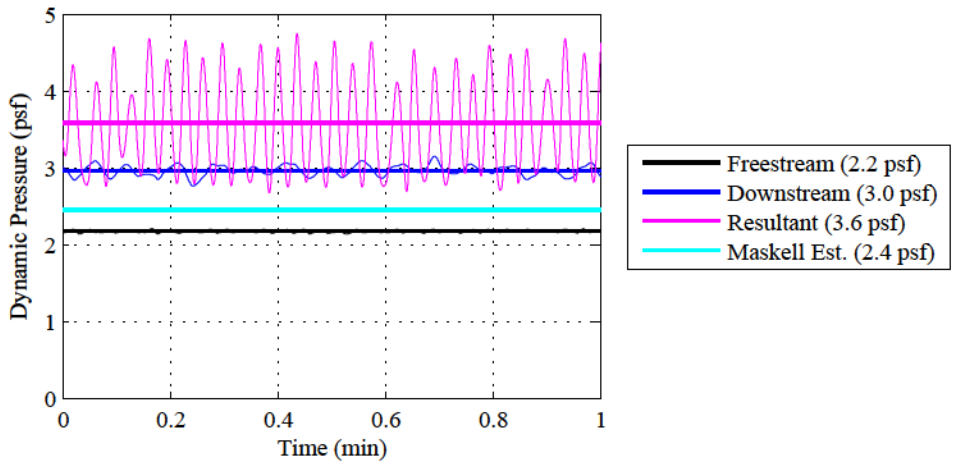

Figure 12: Representative dynamic pressures measurements and calculations for the ringsail canopy are shown. Time-accurate data is shown in the thin solid lines, time-averaged values are shown in the thick solid lines. The average dynamic pressure for each series is also quantified in parentheses in the legend.

Representative dynamic pressures described in this section are shown in Fig. 12 for a one minute data sample at the 25 kt test condition. The freestream dynamic pressure (black line) is nearly constant, indicating a steady freestream condition at the test section inflow boundary. The dynamic pressure measured by the downstream probes (blue line) is approximately 36% higher than the freestream dynamic pressure, which indicates that the parachutes may have caused significantly more blockage than was estimated by Maskell (cyan line). Additionally, the downstream dynamic pressure fluctuated considerably more than the upstream measurement, which is likely due to the oscillation of the canopy, the presence of the strut, and flow turbulence as it has traveled down the test section. The resultant dynamic pressure (magenta line) oscillated at a higher frequency than the downstream dynamic pressure due to the oscillation frequency of the parachute. Additionally, the resultant dynamic pressure spanned a very large range from 2.6 to 4.7 psf, and had an average value that was approximately 64% higher than the freestream measurement. This increase in dynamic pressure at the canopy caused drag loads to be higher than expected. For example, an average C_T in excess of 1.6 and a peak C_T in excess of 2 were obtained when the loads were non-dimensionalized by the freestream dynamic pressure. Non-dimensionalization by the resultant dynamic pressure produced C_T values that were more within accepted values, as shown in Section III.E.

D. Stability Coefficients from Photogrammetry Data

Schoenenberger et al.[7] developed a parameter identification method to extract the static and dynamic stability coefficients as a function of the total AoA from wind tunnel test video data. This method compared very well against static stability coefficients that were determined for the DGB canopy in reference 5. Since this method was developed after the DGB wind tunnel test program was completed, a video image calibration technique was developed using known dimensions from the wind tunnel test fixtures and test articles. This calibration was used to convert pixel data into physical spatial coordinates of the canopy vent and was viewed by the authors as an area that could be significantly improved in future tests. As such, the present wind tunnel test opted to directly measure the location of the canopy vent using stereo photogrammetry instead of inferring the location from video data post-test.

In order to back-calculate the aerodynamic stability coefficients from motion data, it was assumed that the parachute system behaved like a rigid system oscillating about a single pivot point. This one-dimensional parachute model is given in Eq. (6):[7]

$$I_{yy}\ddot{\alpha}_T - C_m q_w S_0 D_0 - m_p g R_{cm} \cos\phi \cos\alpha_T = 0 \tag{6}$$

where I_{yy} is the system's mass moment of inertia (including contributions from both the canopy and the apparent masses) about the point of rotation, m_p is the canopy mass, ϕ is the clock angle of the parachute as shown in Fig. 11, and R_{cm} is the distance from the point of rotation to the system center of mass (cm). The moment coefficient C_m can be decomposed into its static and dynamic components as in Eq. (7).

$$C_m = C_{m_{\dot{\alpha}}} \frac{\dot{\alpha}_T D_0}{2V_w} + C_{m_\alpha}\alpha_T + C_{m_0} = \begin{bmatrix} C_{m_{\dot{\alpha}}} & C_{m_\alpha} & C_{m_0} \end{bmatrix} \begin{bmatrix} \frac{\dot{\alpha}_T D_0}{2V_w} \\ \alpha_T \\ 1 \end{bmatrix} \tag{7}$$

By substituting the vectors in Eq. (7) into Eq. (6) and re-arranging the equation, the stability coefficients can be calculated as in Eq. (8).

$$\begin{bmatrix} C_{m_{\dot{\alpha}}} & C_{m_\alpha} & C_{m_0} \end{bmatrix} = \left(\frac{1}{q_w S_0 D_0}\right)(I_{yy}\ddot{\alpha}_T - mgR_{cm}\cos\phi\cos\alpha_T) \begin{bmatrix} \frac{\dot{\alpha}_T D_0}{2V_w} \\ \alpha_T \\ 1 \end{bmatrix}^\top \left[\begin{bmatrix} \frac{\dot{\alpha}_T D_0}{2V_w} \\ \alpha_T \\ 1 \end{bmatrix} \begin{bmatrix} \frac{\dot{\alpha}_T D_0}{2V_w} \\ \alpha_T \\ 1 \end{bmatrix}^\top \right]^{-1} \tag{8}$$

This method calculates the average stability coefficient set for a given range (or bin) of angle data. The resulting coefficients are assumed to represent the mean total AoA of the data contained within the bin. Coefficients are computed for multiple angles of attack by using a sliding bin. Given the relatively high frequency photogrammetry data taken during testing, the present analysis used a bin size of 0.5° and the bin was slid by 0.25°. As an example, an α_T bin would contain points between 5° and 5.5° (typically over 100 points) and the coefficients would correspond to the mean total AoA within that range. The subsequent bin would contain points between 5.25° and 5.75° α_T. Figure 13 shows representative moment coefficient data calculated from the ringsail canopy motion shown in Fig. 10d. The trim total AoA is shown by the dashed red line. Moment coefficient curves for test articles not shown in Fig. 13 are presented in reference 8.

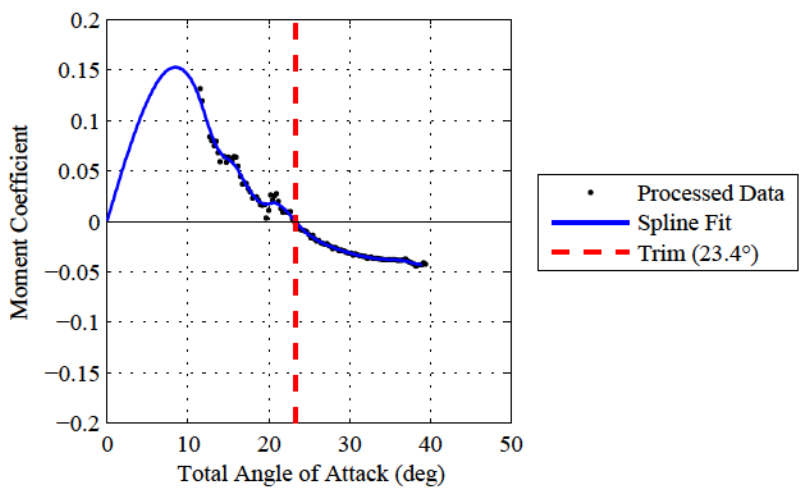

Figure 13: Representative moment coefficient data for the ringsail parachute assuming an apparent inertia coefficient of 0.05. A spline curve fit of the data is shown that is forced to include a zero C_m at a 0° α_T. The trim α_T is also shown.

One of the main sources of uncertainty in Eq. (8) is the moment of inertia term I_{yy}. At sea-level density, the apparent mass in and around the canopy dominates the moment of inertia of the parachute system. The apparent mass (and consequently the apparent inertia) is a difficult value to quantify as it depends on the canopy shape, the porosity of the canopy, the air density, and the air speed. Ibrahim[13] attempted to experimentally quantify the apparent inertia of various rigid parachute canopy shapes and various geometric porosities. The measured apparent inertia coefficients ranged between 0.087 and 0.31 for a ribbon canopy

(26.6% λ_G) and a hemispherical canopy (0% λ_G), respectively. The apparent inertia coefficient is given in Eq. (9).

$$k_{44} = \frac{I_{yy}}{\frac{1}{6}\pi D_p^3 \rho_\infty R_{cm}} \tag{9}$$

For the present analysis, an apparent moment of inertia coefficient of 0.05 was assumed. The authors make no claims as to the correctness of this assumed apparent inertia coefficient, however, and error bounds on the assumed value cannot be estimated. This value is less than the values presented in reference 13, but it created a relatively good correlation with historical C_m data for the DGB canopy presented by in reference 5. The apparent inertia coefficient effectively scales the C_m data shown in Fig. 13 – i.e. larger values of k_{44} increase the values of C_m for a given α_T and vice versa. However, the apparent inertia coefficient value does not appear to affect the trim total AoA.

E. Aerodynamic Coefficient Reduction

All of the aerodynamic coefficients to be presented in Section IV were non-dimensionalized by the resultant dynamic pressure given in Eq. (5). Additionally, the coefficients are all computed with respect to the total AoA, not the total geometric angle. The two aerodynamic coefficients presented in the following results are given in Eq. (10).

$$C_T = \frac{F_T}{q_w S_0} \tag{10a}$$

$$C_m = \frac{M}{q_w S_0 D_0} = C_{m_{\dot{\alpha}}} \frac{\dot{\alpha}_T D_0}{2V_w} + C_{m_\alpha}\alpha_T + C_{m_0} \tag{10b}$$

C_T and C_m were also curve fit with respect to the total angle of attack. The tangential force coefficient was fit using a least-squares third-order polynomial fit and the mean value of all of the C_T data was calculated. The moment coefficient was fit using a spline fit that was forced to pass through zero at 0° total AoA. Representative C_T data is shown in Fig. 14 and representative C_m data is shown in Fig. 13 for the ringsail parachute. In Fig. 14, the scatter in the C_T data for a given total AoA is large, but was typical for all of the canopies. For this particular case, the C_T changes by approximately 37% over the total AoA range and the mean C_T value is shown in red in Fig. 14.

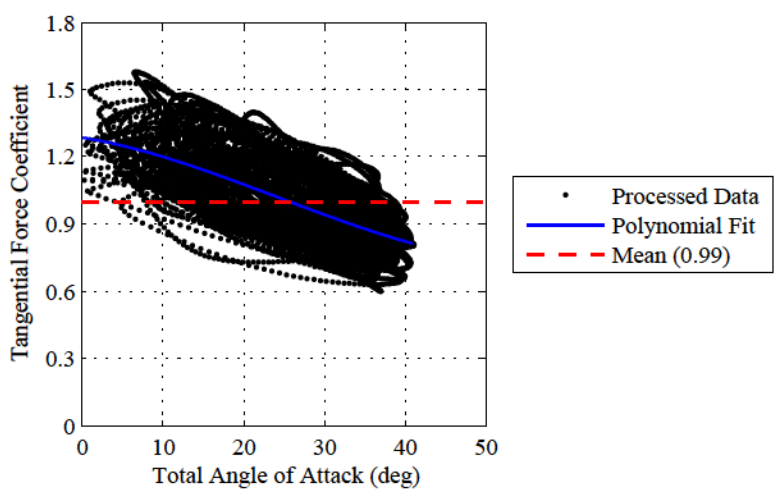

Figure 14: Representative tangential force coefficient data comparing the processed data, the non-linear least squares curve fit, and a mean value.

Figure 14 shows tangential force coefficients greater than 1 throughout a large range of total angles of attack and values as high as 1.5. Parachute literature generally indicates a maximum drag coefficient of 1 for a ringsail parachute, though values of 0.85 and lower are more common. Three activities were performed in order to either support or refute these C_T values. First, load cell accuracy was verified by way of pre-test

and mid-test load checks, in which a second calibrated load cell and independent DAS were attached in-line with the primary load cell. Values from the two load cells were within a few pounds of each other over a large portion of the 5,000 lb_f load cell range in both load check runs, verifying accurate load readings. Second, the tunnel was run without a test article in the tunnel and the downstream q-probe measurements were compared against the upstream q-probe and standard tunnel measurements. The downstream q-probes measured slightly higher than the upstream probes, likely due to flow turbulence and wake effects of the strut, but were otherwise within expected values. Third, the dynamic pressure used in the non-dimensionalization accounts for both blockage and the motion of the parachute, as described in Section III.C. This dynamic pressure is considerably greater than the dynamic pressure measured by the q-probes alone or value estimated by traditional analytical methods. The authors recognize that the tangential force coefficients presented in this work are high relative to generally accepted values, but cannot find rationale to refute the data as presented.

IV. Results and Observations

A. Differences Between Wind Tunnel and Free Flight Behavior

A parachute flying horizontally in a wind tunnel will fly differently than a parachute system in vertical free flight, thus parachute behavior in a wind tunnel cannot always be directly interpreted in terms of its free fight behavior. This is especially true if the wind tunnel testing is performed at a significantly different air density than the flight system. In particular, the parachute oscillatory behavior may be different in a wind tunnel than in free flight due to the inherent differences in the boundary conditions of the system and the apparent mass of the canopy.

A parachute in a wind tunnel is generally restricted from translation and only rotation is permitted due to its attachment to a rigid strut or sting in the test section. This motion is not unlike a pendulum with a fixed support. However, in free flight, the parachute rotates about the system cm and the cm translates in space. This motion is more similar to a pendulum with a moving support. Although the parachute-pendulum analogy isn't precisely accurate, it is representative of the different boundary conditions that exist on the parachute system. And, similar to the two types of pendulums, the two parachute systems can be expected to behave differently.

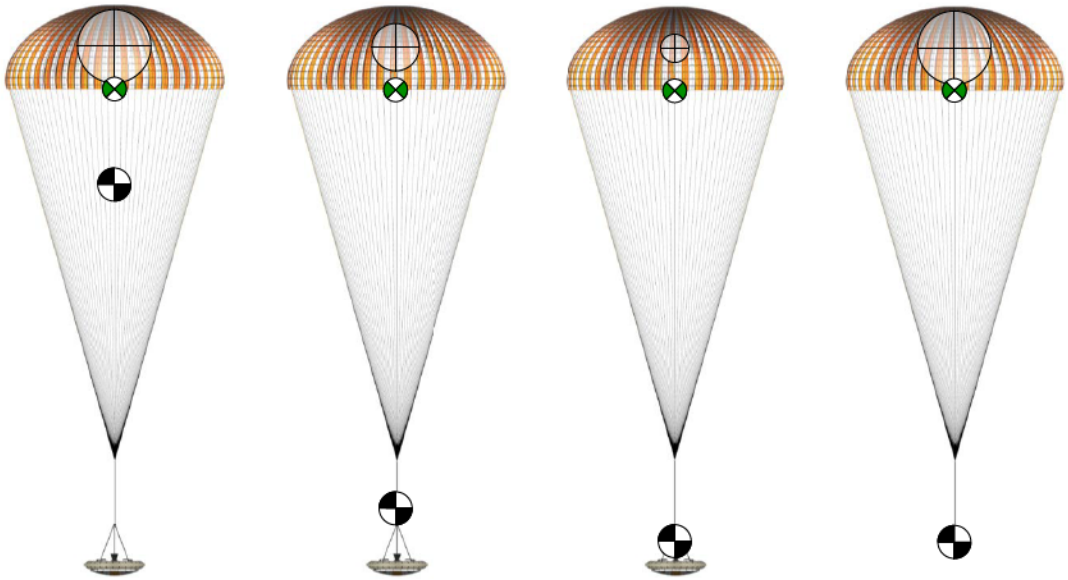

(a) Earth sea-level (b) Earth high-altitude (c) Mars high-altitude (d) Wind tunnel sea-level

Figure 15: Differences in atmospheric density drastically change the relative positions of the system cm (black and white icon) and the parachute cp (green and white icon) as well as the magnitude of the apparent mass (size of the white transparent icon) in both free flight and in a wind tunnel.

The magnitude of the apparent mass scales with the air density, which has a significant effect on where the system cm is located relative to the parachute cp (where the aerodynamic forces are applied, generally located near the skirt of the canopy). Figure 15 shows how the system cm (represented by the black and white icon) changes position relative to the parachute cp (green and white icon) as the magnitude of the apparent mass changes (size of the white transparent icon in the parachute). The moment arm between the system cm and the canopy cp in Fig. 15a is relatively small due to the large apparent mass in the canopy. The moment arm increases at Earth high-altitude and at Mars, Figures 15b and 15c respectively, where the apparent mass is significantly less. Thus, a canopy at Earth high-altitude or at Mars will exhibit higher oscillation angles about the system cm than at Earth sea-level due to the larger moment. Additionally, since the apparent mass is significantly less, the oscillation frequency will be higher at Earth high-altitude and at Mars than at Earth sea-level.

In the NFAC wind tunnel, the parachute is forced to rotate about the ball joint, which simulates an infinite payload mass system and artificially places the cm at the strut. In this configuration, the parachute system has a moment arm similar to the Mars flight system, but an apparent mass similar to Earth sea-level as shown in Fig. 15d. The canopy oscillation amplitude will be relatively large due to the long moment arm and the high apparent inertia. However, the high apparent inertia will also damp the oscillation and result in a lower oscillation frequency than the Mars flight system.

Given the differences in the boundary conditions and apparent mass arrangements shown in Fig. 15, it would be difficult to replicate free flight behavior in a wind tunnel operating at sea-level air densities. As such, *the parachute behavior in the present wind tunnel test is not expected to replicate free flight behavior.* An underlying assumption in conducting these wind tunnel experiments is that the relative differences between canopy behaviors should remain the same in a different environment. In other words, if canopy A has better stability properties than canopy B in a wind tunnel at sea-level density, then canopy A should have better stability properties than canopy B in free flight at Mars. This assumption was vetted and agreed upon by parachute industry experts and is a primary justification for performing the canopy comparison and down-selection using the NFAC wind tunnel.

If the air density cannot be changed, however, similarity to free flight may increase if the test article size is decreased. Parachute motion is a result of the aerodynamic forces acting on the canopy and the apparent mass. Assuming that the apparent mass dominates, Newton's Second Law can be written in terms of angular motion as in Eq. (11).

$$\dot{\omega} = \frac{M}{I_{yy}} = \frac{C_N q \frac{\pi}{4} D_0^2 R_{cp}}{k_{44} \frac{\pi}{6} D_p^3 \rho_\infty R_{cm}} \sim \frac{1}{\rho_\infty D_0} \tag{11}$$

The moment acting on the canopy scales with the square of the canopy's diameter where as the apparent mass scales with the cube of the canopy's diameter. Thus, for a sea-level wind tunnel test, the ratio of the canopy force to its apparent mass for a small test article would be closer to a high-altitude flight system ratio than for a large test article. This increase in flight system similarity can be inferred from the sub-scale parachute testing in reference 5, which was performed at sea-level air densities but used test articles with a nominal diameter of 5.2 ft.

B. Comparative Data Metrics

The drag performance and stability of each canopy were comparatively assessed based on a set of three metrics: the average tangential force coefficient, the amplitude of canopy oscillation, and the trim total angle of attack. The average tangential force coefficient across the total angle of attack range was used to represent the drag performance of each canopy. Note that C_T was *not* constant and varied with α_T for each canopy, but it was not always effective to compare many different canopy configurations based on a set of curves.

The amplitude of canopy oscillation was represented by the 95th percentile of the total AoA. The 95th percentile total AoA was selected because occasional random behavior caused the maximum total AoA to be uncharacteristically high for a given canopy within the data sample duration. The trim total AoA is an important measure of the stability of a canopy as the canopy will theoretically oscillate or cone near this angle. A small trim total AoA is desirable as this will apply canopy forces more through the center of the payload and prevent large coning angles, which can complicate ground acquisition measurements in flight. The trim total AoA was determined from the estimated C_m data.

C. Effect of Material Permeability

Two DGB canopies were flown during this test program. One DGB was a spare unit leftover from the Mars Phoenix mission, which was constructed from MIL-C-7020 Type I nylon. A second DGB was built as a Phoenix DGB replica except that it was constructed using the F-111 nylon. As previously stated, the difference in permeability between MIL-C-7020 and F-111 nylon has been shown to be inconsequential in a low-density environment and the two DGB canopies should theoretically behave similarly at Mars. However, in high-density environments (such as the NFAC test environment, which is located approximately at sea-level), the material permeability can significantly contribute to the total porosity of the canopy. There are varying data sets regarding the permeability of MIL-C-7020 as well as different ways of computing the material permeability contribution to the total porosity. Thus, the total porosity of the MIL-C-7020 DGB can ranged between 15% and 18%. The permeability of the F-111 material was assumed to be negligible, thus the total porosity of the F-111 DGB is equal to its geometric porosity of 13%.

Switching to an imporous material increased the oscillation amplitude of the DGB canopy by approximately 86%, increased the trim AoA by 120%, and increased the mean tangential force coefficient by 37%. These results are not entirely surprising as similar behavior in the canopy drag and stability for two material permeabilities was also observed in reference 5. However, it is not apparent to the authors that increasing the geometric porosity of the F-111 DGB to match the total porosity of the MIL-C-7020 DGB (by increasing the gap or vent size or cutting holes in the broadcloth) will render similar drag and stability behavior. Distributed porosity in the form of material permeability is believed to affect the drag and stability of the parachute differently than discrete porosity changes, implying that two canopies of equal total porosity may behave differently depending on how the porosity is distributed throughout the canopy.

The average drag and stability performance of the two DGBs are summarized in Table 3. To make an appropriate comparison, the ringsail and ringsail-derivative canopies metrics presented in the subsequent sections were compared against the F-111 DGB only.

Table 3: DGB drag and stability metric summary.

Image		
Broadcloth Material	MIL-C-7020 Type I nylon	PIA-C-44378 F-111 nylon
Canopy No.	DGB-1	DGB-2
Total Porosity	15-18%	13%
Mean C_T	0.59	0.81
95th Percentile α_T	17°	31°
Trim α_T	8°	18°

D. Ringsail Results

Going into the wind tunnel test, the ringsail canopy was anticipated to be the preferred canopy type to replace the DGB as the next-generation Mars supersonic parachute. The ringsail offers a host of advantages over the DGB including increased canopy robustness, increased inflation reliability at large diameters, higher subsonic drag, and the ability to be reefed to limit opening loads or increase stability. However, it is generally true that parachutes with high drag also have relatively poor stability and vice versa. Thus, the goal of the ringsail testing was to explore the geometric porosity distribution design space and determine the trade-off between drag and stability. A summary of the ringsail canopy configurations, their designation numbers, and their data metrics is given in Table 4.

The ringsail RS-0 canopy exhibited significant oscillation, sometimes nearly touching the floor and ceiling of the test section. The 95th percentile total geometric angle was approximately 20°. It is not known if the

Table 4: Ringsail drag and stability metric summary.

Image	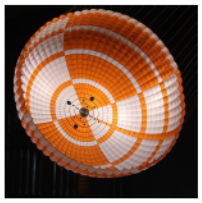				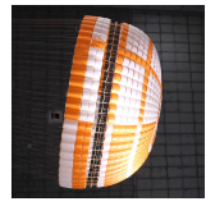
Canopy Mod	None	2/3 of ring 19 removed	27% of rings 17, 18, and 19 removed	All of ring 19 removed	All of rings 18 and 19 removed
Canopy No.	RS-0	RS-1	RS-2	RS-3	RS-4
λ_G	10%	13%	15%	16%	22%
Mean C_T	0.99	0.90	0.91	0.86	0.77
95th %tile α_T	39°	35°	35°	33°	31°
Trim α_T	24°	23°	21°	21°	19°

total geometric angle would have been greater if not for the presence of the test section walls. The oscillation frequency was approximately 0.5 Hz at the 25 kt condition and approximately 0.3 Hz at the 15 kt condition, but the oscillation amplitudes were approximately equal for both test conditions. Due to the relatively high rotational velocity of the canopy, the panels in rings 20-22 tended to flutter when the canopy approached the center of the test section (when its rotational velocity was the highest). This sail panel flutter can be seen in Fig. 16 and was present to some degree in all of the ringsail configurations tested. Each of the comparisons quoted in this section are referenced to the RS-0 canopy (unless otherwise noted).

Figure 16: Sail panel flutter due to canopy rotation in the test section.

Canopy RS-1 was created to mimic the geometric porosity and distribution of the modified ringsail tested during the Planetary Entry Parachute Program (PEPP) in 1967.[14] This modification decreased the angle excursion by about 9%, but decreased the drag coefficient by about 9% as well. Instead of concentrating all of the porosity in one ring, as in the PEPP ringsail and RS-1, canopy RS-2 distributed that same porosity over rings 17, 18, and 19. This was done in hopes of creating flow disturbance at multiple points along the canopy. However, it decreased the angle excursion and drag coefficient equally by approximately 8%.

In testing canopy RS-1, the partial sail in ring 19 appeared to flutter nearly constantly due to the canopy's motion and did not appear to significantly contribute to the drag or stability of the canopy. Thus, the partial

panels in ring 19 were removed to create canopy RS-3. The contribution of the small panels were greater than expected, resulting in a 6% decrease in the angle excursion and a 4% decrease in drag relative to canopy RS-1.

Finally, in an attempt to mimic the "gap-band" portion of a DGB parachute, all of ring 18 was removed, which effectively made rings 20-22 a "band" and rings 18-19 a "gap". This configuration, canopy RS-4, performed poorly overall, exhibiting a 22% decrease in the average drag and a 21% decrease in the angle excursion. With both rings 18 and 19 removed, the canopy's projected diameter appeared to be smaller than in previous configurations when the test article was observed in flight. This decrease in the projected diameter was likely due to the significant decrease in the internal pressure near the skirt of the canopy, which would subsequently cause the large observed decrease in the tangential force coefficient. Additionally, without the support of the sails in rings 18 or 19, the "sail band" in rings 20-22 tended to move independently from the rest of the canopy and tended to take a more amorphous shape than a circular shape.

E. Disksail Results

Table 5: Disksail drag and stability metric summary.

Image		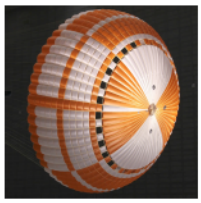			
Canopy Mod	None	Every other panel in ring 11 removed	All of ring 11 removed	All or ring 11 and every other panel in ring 17 removed	All of ring 11, every other panel in rings 17 and 18 removed
Canopy No.	DS-0	DS-1	DS-2	DS-3	DS-4
λ_G	9%	11%	13%	16%	19%
Mean C_T	1.03	0.98	0.92	0.86	0.82
95th %tile α_T	38°	36°	32°	31°	28°
Trim α_T	23°	18°	14°	12°	14°

The disksail concept emerged from the desire to close off the geometric porosity in the ringslot portion of the ringsail canopy, which ultimately reduced the geometric porosity by approximately 1% due to the slightly larger vent (see Table 2). It should be reiterated that the disk portion of the canopy was fabricated as a flat disk (due to time constraints) where a ringsail is typically hemispherical in shape. In flight, the flat disk caused the back side of the parachute to be more blunt than the ringsail and caused the canopy to appear slightly more boxy rather than hemispherical. This shape change, in addition to the slightly lower geometric porosity, increased the tangential force coefficient by 4% and decreased the oscillation amplitude by approximately 2% relative to canopy RS-0. This means that the disksail effectively accomplished an increase in drag with a simultaneous increase in stability. However, a larger increase in the stability of the system was desired.

Given that the disksail and ringsail are similar canopies, it was assumed that modifications in the skirt region of the ringsail would have similar effects on the disksail. Thus, there was a desire to investigate the effect of opening geometric porosity near the crown of the parachute. Additionally, it was hoped that pressure recovery of the disk portion of the parachute would create stronger air flow through gaps near the crown. Thus, canopies DS-1 and DS-2 were created, in which every other panel and all of ring 11 (just

below the disk) was removed, respectively. Canopy DS-1 decreased both the drag and angle excursions by approximately 5%. However, cutting out all of ring 11 caused almost a 15% decrease in the angle excursion with only an 11% decrease in the drag coefficient, relative to canopy DS-0. Oscillation frequencies were 0.5 Hz and 0.3 Hz for the 25 kt and 15 kt test conditions, respectively, similar to the ringsail.

From the ringsail testing, it was clear that removing two whole rings of sails caused an undesired decrease in the projected diameter and drag of the parachute. However, it is believed that at supersonic speeds, it will be necessary to have porosity near the shoulder of the canopy to aid in stability. As such, every other panel in ring 17 and subsequently every other panel in ring 18 was cumulatively removed (in addition to all of ring 11 having already been removed removed) to create canopies DS-3 and DS-4, respectively. By removing every other panel in ring 17 along with all of ring 11, the tangential force coefficient decreased by 16.5%, but the oscillation magnitude decreased by 19.5%, relative to canopy DS-0. Canopy DS-4 exhibited a decrease in C_T by approximately 20% and a decrease in the angle excursion by over 26%. All of the disksail configurations are shown in Table 5.

Although the addition of porosity near the crown (specifically, in ring 11) appeared to benefit the stability of the parachute, it is not known how adding geometric porosity in this manner will affect the opening behavior of the parachute at supersonic Mach numbers. In one example, the modified ringsail parachute tested as part of PEPP did not properly inflate at a Mach number of 1.64, which the authors concluded was due to excessive total porosity in the crown of the canopy.[14] However, the material in the crown of the parachute had a nominal permeability of 700 $ft^3/min/ft^2$, which is significantly greater than typical parachute material permeability and considerably increased the total porosity of the crown. Additionally, NASA's Capsule Parachute Assembly System program has demonstrated that ringsail canopies will successfully inflate at subsonic Mach numbers with a ring of added geometric porosity near the crown.[15]

The cumulative modifications performed on the disksail were more effective (i.e. increased the stability more than it decreased the drag of the canopy) than the modifications performed on the ringsail. It is also believed that these modifications should have very similar effects when implemented on a ringsail canopy. However, it should be noted that a final flight article may not be constructed as the disksail was constructed for this test. There is a reliability advantage in retaining the ringsail skeletal structure near the crown in that it may help prevent a catastrophic failure of the canopy in the event of damage. The slight mass savings and performance gain of a flat circular disk at the crown of the canopy are not significant enough to sacrifice this robustness advantage. Additionally, the geometric porosity of the disksail in the crown (or rather, the lack of geometric porosity) can be approximated by reducing the slot size in the Ringslot portion of the canopy to near zero.

F. Starsail Results

The starsail was an experiment to recover more geometric porosity than the disksail by replacing several gores of the ringsail canopy with solid sheets of F-111 material. The skeletal structure of the ringsail canopy remained the same, but six groups of four solid gores (24 solid gores total) were sewn into the structure instead of discrete sails. The hope with this canopy was that the solid gores would function similarly to a cross parachute and generate increased flow energy out of the remaining sails to aid in stabilization. The porosity recovered by the solid gores was moved to the shoulder of the canopy by adding small gaps to the leading edge of rings 17-20, increasing the geometric porosity to approximately 13% (approximately equal to the DGB).

In flight, the starsail's projected shape appeared more like a six-sided polygon rather than circular, which may be due to two factors. First, the solid gores were fabricated on a flat circular planform rather than a quarter-hemispherical (which is typical for a ringsail) due to time constraints in fabricating the starsail. Second, the solid gores likely experienced higher internal pressurization as compared to the vented sail gores, which would increase the outward force on those gores. Both the gore geometry discrepancy and the non-uniform radial force on the gores could cause the canopy to take a non-circular shape.

Ultimately, the starsail did not perform as well as the ringsail or disksail designs. With respect to the base ringsail RS-0 performance, the tangential force coefficient decreased by 16% and the oscillation amplitude decreased by only 9%. Due to its relatively poor performance and difficult construction, the starsail was not considered for further modification.

Table 6: Starsail drag and stability metric summary.

Image	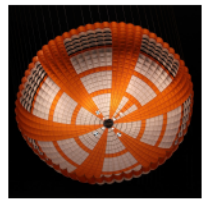
Canopy No.	SS
Total Porosity	13%
Mean C_T	0.83
95th Percentile α_T	35°
Trim α_T	24°

G. Canopy Comparisons

As previously stated, the goal of this wind tunnel test was to experiment with different canopy configurations and geometric porosity distributions to find a configuration that yielded better drag than the DGB with equivalent or better stability. Figure 17 shows the tangential force coefficient and the 95th percentile total AoA for each of the tested canopies normalized with respect to the performance of the F-111 DGB. Ideal configurations would appear above and to the left of the black DGB-2 symbol. Canopy DS-3 (all of ring 11 and every other panel in ring 17 removed) would be good candidate as it increased the drag coefficient by 6% and decreased the oscillation amplitude by 2%. However, canopy DS-2 (all of ring 11 removed) may be a better candidate as it increased the drag coefficient by 14% and only resulted in a 4% increase in the oscillation amplitude (which may be interpreted as equivalent stability).

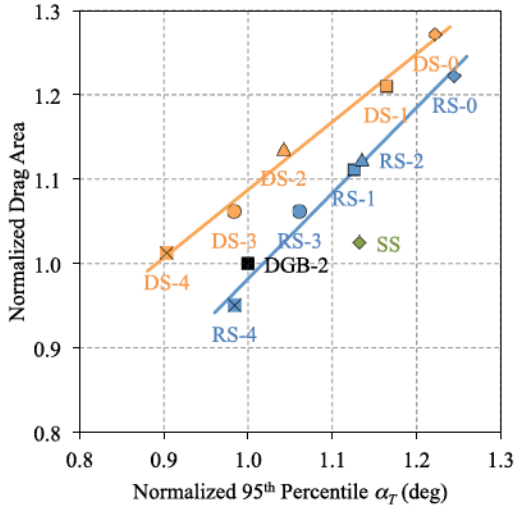

Figure 17: Comparison of all of the tested canopy configurations normalized with respect to the performance of the F-111 DGB.

It is interesting to note that all of the modifications of a given canopy type tended to alter the ratio of the drag-to-stability in a linear fashion. This implies that altering the geometric porosity via removal of sail panels tends to decrease the drag and increase the stability of the parachute in the same relative ratio, but that ratio differs for different types of canopies.

All geometric porosity is not created equal, however, meaning that the drag coefficient and the stability of the canopy can be drastically different for different canopies of equal geometric porosity. Figure 18a shows that the tangential force coefficient changes linearly with the geometric porosity, with the exception of the

starsail and the DGB. Additionally, for an equivalent geometric porosity, the DGB had a lower tangential force coefficient than the starsail and a significantly lower C_T than the ringsail (linearly inferred from the ringsail and disksail data).

Unlike the tangential force coefficient, the trim total AoA does not appear to have a direct correlation with the geometric porosity, as shown in Fig. 18b. For example, canopies RS-1 and RS-2 have the same geometric porosity and vary in their trim AoA by approximately 2°. On a basis of the trim total AoA, canopies DS-2 and DS-3 appear very appealing similar to the conclusion drawn from Fig. 17.

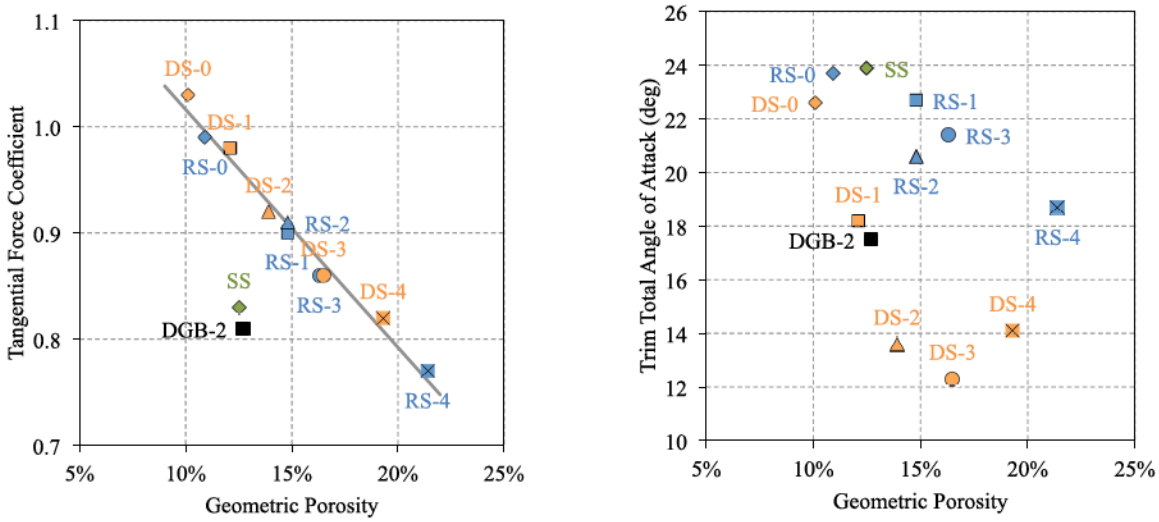

(a) Tangential force coefficient

(b) Trim total angle of attack

Figure 18: Geometric porosity effect on the tangential force coefficient and the trim total angle of attack.

V. Conclusions

Thirteen different types of sub-scale canopy configurations were tested in the NFAC 80x120 test section that were derived from four major parachute structural designs. Load cell, dynamic pressure, and photogrammetric data were taken in order to quantify the relative drag and stability of each parachute design. The tangential force coefficient was used as a surrogate for the drag coefficient. The stability of each article was evaluated using the trim total angle of attack and the 95th percentile total angle of attack (to represent the maximum angular excursion). Testing of two DGB canopies using materials of different permeabilities illustrated the relatively large effect of material permeability in testing at approximately sea-level air densities. Since the ringsail and ringsail-derivative canopies were fabricated from low permeability F-111 nylon, the low permeability DGB performance (mean C_T of 0.81, 95th α_T 21°) was used as a baseline reference to assess the relative goodness of a particular configuration. The overall goal was to examine various geometric porosity configurations on the ringsail and ringsail-derivative canopies to obtain greater drag than the DGB with equivalent or better stability.

Five different ringsail configurations were tested with geometric porosities ranging from 11% to 21% that involved removing various sail panels from rings 17-20. However, these canopy modifications did not yield an acceptable change in the C_T and the excursion angle relative to the F-111 DGB to be particularly attractive. Trim total angles of attack were also larger than the F-111 DGB. Five disksail configurations were tested with geometric porosities ranging from 10% to 19% that involved removing various sail panels from rings 11, 17, and 18. The combination of the flat disk, removal of all of ring 11, and removal of every other panel in ring 17 (canopy DS-3) resulted in a slightly higher C_T than the F-111 DGB (approximately 6% higher) as well as better stability. A significantly higher average C_T (approximately 14%) was obtained when only ring 11 was removed from the disksail (DS-2) with only a relatively small increase in the angle excursion (approximately 4% increase). This makes both DS-2 and DS-3 good candidates relative to the F-111 DGB performance. Only one starsail configuration was tested and it did not result in improved performance above the DGB.

This wind tunnel test program generated a wealth of data and a large portion of that data is still being processed. Not all of the parachute configurations tested during this test program are presented in this manuscript. Additionally, one final test entry was performed in which many promising canopy configurations were tested, but those data were not available in time for this publication. There remain some issues regarding the data set that deserve additional attention, such as the relatively high C_T values, the relatively high blockage measurements, and how to properly interpret wind tunnel behavior in a high-density environment in the context of free flight behavior in a low-density environment. It is the hope of the authors that the data in this manuscript will inspire useful comments and insight on these issues from the greater parachute community. Forward progress on the full-scale supersonic parachute is being made. LDSD has initiated the fabrication of a full-scale ringsail skeletal structure designed for 150,000 $\mathrm{lb_f}$ limit load. The final canopy configuration, to be selected at a later time, can be sewn into this structure for Parachute Design Verification and Supersonic Flight Dynamics tests that are currently proposed to occur within the next two years.

Acknowledgements

The Low Density Supersonic Decelerator project is directed by the Jet Propulsion Laboratory, California Institute of Technology, under a contract with the National Aeronautics and Space Administration. The authors would like to acknowledge the exceptional work performed by NFAC Test Director Patrick Goulding II, NFAC Facility Manager Joe Sacco, and the NFAC crew in assuring that this test was performed safely, efficiently, and within budget. The NFAC facility and personnel exhibited exceptional professionalism and flexibility with regards to augmentation of the test program objectives. Acknowledgement is also owed to Laura Kushner, Edward Schairer, and JT Heineck in the Experimental Aero-Physics Branch at NASA Ames Research Center. They designed, installed, calibrated, and operated a high-accuracy multi-camera photogrammetric system in the 80x120 within a compressed schedule. They also supplied and integrated the high-resolution color cameras, promptly provided processed data, and archived all video data acquired for the test program. The authors would like to acknowledge JPL personnel Doug Adams and Cassandra Mercury for their invaluable assistance in organizing and executing this test program as well as developing valuable parachute configurations. Acknowledgement is due to the parachute engineers, technicians, and sewers at Pioneer Aerospace for their dedication and long work hours to turn around test article modifications within very small time frames. The authors would like to acknowledge Keir Gonyea and Mark Schoenenberger for their efforts in developing the methods and routines to perform the data reduction. Finally, the authors would like to thank Juan Cruz, Elsa Hennings, and Dean Wolf for their consultation regarding canopy configurations and observed parachute behavior.

References

[1]McBride, D. D., "Orbiter Drag Chute Stability Test in the NASA Ames 80x120 Foot Wind Tunnel," Tech. Rep. SAND-93-2544, Sandia National Laboratories, Albuquerque, NM, Feb. 1994.

[2]Witkowski, A., Machalick, W., and Taeger, Y., "Mars Subsonic Parachute Technology Task System Overview," *18th AIAA Aerodynamic Decelerator Systems Technology Conference and Seminar,* AIAA 2005-1657, Munich, Germany, May 2005.

[3]Mitcheltree, R., Burno, R., Slimko, E., Baffes, C., Konefat, E., and Witkowski, A., "High Altitude Test Program for a Mars Subsonic Parachute," *18th AIAA Aerodynamic Decelerator Systems Technology Conference and Seminar,* AIAA 2005-1659, Munich, Germany, May 2005.

[4]Gallon, J. C., Clark, I. G., Rivellini, T. P., Adams, D. S., and Witkowski, A., "Low Density Supersonic Decelerator Parachute Decelerator System," *22nd AIAA Aerodynamic Decelerator Systems Technology Conference and Seminar*, Daytona Beach, FL, March 2013.

[5]Cruz, J. R., Mineck, R., Keller, D., and Bobskill, M., "Wind Tunnel Testing of Various Disk-Gap-Band Parachutes," *17th AIAA Aerodynamic Decelerator Systems Technology Conference and Seminar,* AIAA 2003-2129, Monterey, CA, May 2003.

[6]Lingard, J. S. and Underwood, J., "The Effect of Low Density Atmospheres on the Aerodynamic Coefficients of Parachutes," *13th AIAA Aerodynamic Decelerator Systems Technology Conference,* AIAA 1995-1556, Clearwater Beach, FL, May 1995.

[7]Schoenenberger, M., Queen, E. M., and Cruz, J. R., "Parachute Aerodynamics from Video Data," *18th AIAA Aerodynamic Decelerator Systems Technology Conference and Seminar,* AIAA 2005-1633, Munich, Germany, May 2005.

[8]Gonyea, K. C., Tanner, C. L., Clark, I. G., Kushner, L. K., Schairer, E. T., and Braun, R. D., "Aerodynamic Stability and Performance of Next-Generation Parachutes for Mars Entry, Descent, and Landing," *22nd AIAA Aerodynamic Decelerator Systems Technology Conference and Seminar*, Daytona Beach, FL, March 2013.

[9]Maskell, E. C., "A Theory of the Blockage Effects on Bluff Bodies and Stalled Wings in a Closed Wind Tunnel," Tech. Rep. Reports and Memoranda No. 3400, Ministry of Aviation, Nov. 1963.

[10]Macha, J. M. and Buffington, R. J., "Wall-Interference Corrections for Parachutes in a Closed Wind Tunnel," *Journal of Aircraft*, Vol. 27, No. 4, April 1990, pp. 320–325.

[11]Knacke, T. W., *Parachute Recovery Systems Design Manual*, Para Publishing, 1st ed., 1992.

[12]Zell, P. T., Cruz, J. R., and Witkowski, A., "Structural Testing of Parachutes in the National Full-Scale Aerodynamics Complex 80-by-120-Foot Wind Tunnel at NASA Ames Research Center," *17th AIAA Aerodynamic Decelerator Systems Technology Conference and Seminar,* AIAA 2003-2130, Monterey, CA, May 2003.

[13]Ibrahim, S. K., "Experimental Determination of the Apparent Moment of Inertia of Parachutes," Tech. Rep. AFFDL-TDR-64-153, Air Force Flight Dynamics Laboratory, Wright-Patterson Air Force Base, Ohio, April 1965.

[14]Eckstrom, C. V., Murrow, H. N., and Preisser, J. S., "Flight Test of a 40-Foot-Nominal-Diameter Modified Ringsail Parachute Deployed at a Mach Number Of 1.64 and a Dynamic Pressure of 9.1 Pounds Per Square Foot," Tech. Rep. NASA TM X-1484, NASA Langley Research Center, Hampton, VA, Nov. 1967.

[15]Morris, A. L., Bledsoe, K. J., Fraire, U., Moore, J. W., Olsen, L. M., and Ray, E. S., "Summary of CPAS Gen II Testing Analysis Results," *21st AIAA Aerodynamic Decelerator Systems Technology Conference,* AIAA 2011-2585, Dublin, Ireland, May 2011.